

Ultrafast demagnetization dynamics of 4f antiferromagnets

Maryna Pankratova ^{1,2,3,*} Vladislav Borisov ^{2,3} Danny Thonig ^{2,4} Rohit Pathak ² Yoav William Windsor ^{5,6}
 Laurenz Rettig ⁵ Olle Eriksson ^{2,3} Arthur Ernst ^{7,8,9} and Anders Bergman ^{2,3}

¹Department of Engineering Sciences, *University of Skövde*, SE-541 28 Skövde, Sweden

²Department of Physics and Astronomy, *Uppsala University*, Box 516, SE-75120 Uppsala, Sweden

³Wallenberg Initiative Materials Science for Sustainability, *Uppsala University*, 75121 Uppsala, Sweden

⁴School of Science and Technology, *Örebro University*, SE-701 82 Örebro, Sweden


⁵Department of Physical Chemistry, *Fritz Haber Institute of the Max Planck Society*, Faradayweg 4-6, 14195 Berlin, Germany

⁶Institut für Physik und Astronomie, *Technische Universität Berlin*, Straße des 17 Juni 135, 10623 Berlin, Germany

⁷Institute for Theoretical Physics, *Johannes Kepler University*, Altenberger Strasse 69, 4040 Linz, Austria

⁸Max-Planck-Institut für Mikrostrukturphysik, Weinberg 2, 06120 Halle (Saale), Germany

⁹Donostia International Physics Center (DIPC), 20018 Donostia-San Sebastián, Spain

 (Received 23 January 2025; revised 6 July 2025; accepted 26 August 2025; published 18 September 2025)

We study the ultrafast demagnetization dynamics of $LnRh_2Si_2$ ($Ln = Pr, Nd, Sm, Gd, Tb, Dy, Ho$) antiferromagnets after excitation by a laser pulse, using a combination of density functional theory and atomistic spin and spin-lattice dynamics simulations. In the first step, we calculate the Heisenberg interactions using the magnetic force theorem and compare two approaches, where the 4f states of the rare earths are treated as frozen core states or as valence states with added correlation corrections. We find marked quantitative differences in terms of predicted Curie temperature for most of the systems, especially for those with a large orbital moment of the rare-earth cations. This can be attributed to the importance of indirect interactions of the 4f states through the Si states, which depends on the binding energy of the 4f states and coexists with Ruderman-Kittel-Kasuya-Yosida-type interactions mediated by the conduction states. However, qualitatively both approaches agree in terms of the predicted antiferromagnetic ordering at low temperature, which is in line with previous experiments. In the second step, the atomistic dynamics simulations are used in combination with a heat-conserving two-temperature model, which allows for the calculation of spin and electronic temperatures during the magnetization dynamics simulations. Our simulations demonstrate that despite quite different demagnetization times, magnetization dynamics of all studied $LnRh_2Si_2$ antiferromagnets exhibit similar two-step behavior, in particular the first fast drop followed by slower demagnetization. In addition, we observe that the demagnetization amplitude depends linearly on laser fluence, for low fluences, something that is also in agreement with experimental observations. We also investigate the impact of lattice dynamics on ultrafast demagnetization using coupled atomistic spin-lattice dynamics simulations and the heat-conserving three-temperature model, which confirm the linear dependence of magnetization on laser fluence. The microscopic mechanisms behind these behaviors are investigated in detail.

DOI: [10.1103/rjvq-qs9x](https://doi.org/10.1103/rjvq-qs9x)

I. INTRODUCTION

The field of ultrafast magnetization dynamics was launched in 1996 with the work of Beaurepaire *et al.* [1], who studied the impact of the femtosecond laser pulse on the demagnetization of Ni films and demonstrated for the first time ultrafast demagnetization on subpicosecond timescales. Ultrafast demagnetization can be very useful for prospective spintronic devices since it could allow switching of magnetization on picosecond timescales, addressing the demand

for a growing data storage speed. While ultrafast demagnetization was first observed in nickel [1,2], numerous studies have followed, including ferromagnetic (FM) [3–8] and ferromagnetic materials [9]. However, for spintronic applications, antiferromagnetic (AFM) materials form perhaps an even more promising class of magnets [10–12], due to properties such as a robustness against external magnetic perturbations. In addition, an experimental study comparing FM and AFM ultrafast demagnetization for Dy reported that quenching of magnetization is faster and more efficient for the AFM phase than for the FM one [13]. Moreover, while comparing FM and AFM order between FeGd sublattices, it was theoretically predicted that AFM coupling of the sublattices accelerates the demagnetization of both sublattices [14].

Recently, the ultrafast demagnetization of a series of lanthanide-based 4f antiferromagnets was systematically studied experimentally in Ref. [10]. The considered materials were prepared specifically to possess similar lattice and magnetic structure, allowing us to focus solely on the impact

*Contact author: maryna.pankratova@his.se, maryna.pankratova@physics.uu.se

Published by the American Physical Society under the terms of the [Creative Commons Attribution 4.0 International license](https://creativecommons.org/licenses/by/4.0/). Further distribution of this work must maintain attribution to the author(s) and the published article's title, journal citation, and DOI. Funded by [Bibsam](https://www.bibsam.com/).

of $4f$ occupation. It was demonstrated that the timescales of the demagnetization dynamics can differ up to two orders of magnitudes; however, the angular momentum transfer rates scale linearly with the de Gennes factor $G = (g_J - 1)^2 J(J + 1)$, where g_J and J are the Landé factor and the total $4f$ angular momentum quantum number, respectively. In addition, density functional theory (DFT) calculations were performed in Ref. [10] to obtain the corresponding exchange interaction values. Details on the correct description and methodology for the localized $4f$ electrons were not provided in Ref. [10] and will be discussed here.

In Ref. [10], it was found that coupling between the nearest antiferromagnetically aligned spins also scales linearly with the de Gennes factor. Moreover, it was shown that the demagnetization amplitude increases linearly with laser fluence for all studied systems, which agrees with previous experimental observations for other materials (see Refs. [7,11] and references therein). It should be noted that magnetization dynamics studies were not performed in Ref. [10] to confirm that the simulated demagnetization amplitude based on such interactions depends linearly on laser fluence, and filling in this theoretical gap is the focus of the present work.

Theoretically, ultrafast magnetization dynamics is often interpreted using two- or three-temperature models [1,2,12]. These models usually include two or three coupled reservoirs, i.e., spin, electron, and lattice. In the three-temperature model (3TM) proposed by Beaurepaire [1], there are several coupling constants that are responsible for the transfer of heat between the subsystems: electron-phonon G_{ep} , electron-spin G_{es} , and spin-lattice G_{sl} . These constants for $3d$ ferromagnets, such as iron, cobalt, and nickel, are estimated in various works with up to one order of magnitude difference [2,3,7], which impedes the theoretical interpretations of experimental observations. In addition, the 3TM proposed by Beaurepaire fails to describe demagnetization on subpicosecond timescales. Recently, a heat-conserving three-temperature model (HC3TM) was proposed [2], where Gilbert and lattice dampings govern a coupling between the electron, lattice, and spin degrees of freedom. These values can be calculated *ab initio*, and they can thus facilitate a comparison between experiment and calculations more accurately and are less dependent on empirical parameters. Moreover, the HC3TM results in a qualitatively correct description of the demagnetization dynamics on subpicosecond timescales for all $3d$ ferromagnets [2,7]. Building on these successes, the HC3TM is a promising candidate for a more realistic description of demagnetization times on subpicosecond timescales also in the $LnRh_2Si_2$ series, where the quite significant differences in demagnetization times, especially the fast demagnetization of $SmRh_2Si_2$, are making the 3TM of Ref. [1] questionable, especially facing the difficulty of identifying several coupling constants needed in this model: G_{ep} , G_{es} , G_{sl} .

In this work, we report DFT calculations of exchange interaction parameters for $LnRh_2Si_2$ and atomistic spin dynamics simulations of ultrafast demagnetization dynamics combined with the heat-conserving two- and three-temperature models. The paper is organized as follows. First, we present the results of density functional theory calculations. Then, the calculated parameters are used in atomistic spin and spin-lattice dynam-

ics simulations to study ultrafast demagnetization dynamics and the impact of laser fluence and lattice dynamics on magnetization dynamics of lanthanide-based antiferromagnets.

II. METHODS

A. First principles density functional theory

In the first step, we calculate the electronic properties of the rare-earth compounds $LnRh_2Si_2$ based on the measured crystal structure, using two different approaches: (i) all-electron full-potential fully relativistic electronic structure software RSPt [15,16], and (ii) a fully relativistic multiple scattering Green's function method theory formulated in the Korringa-Kohn-Rostoker approach and implemented in the code hutsepot [17,18].

In (i), the electronic structure is described on the level of density functional theory within the generalized-gradient approximation in Perdew-Burke-Ernzerhof (PBE) parametrization. Smearing of 1 mRy is used for electronic occupations, and a $(40 \times 40 \times 16)$ k -mesh is used for sampling the Brillouin zone. An AFM structure is imposed in our calculations, where each Ln layer is ferromagnetic, but neighboring layers are AFM-coupled, which is close to the measured magnetic ground states of the studied rare-earth compounds. We have also tested the FM structure, but the calculated magnetic coupling parameters indicate AFM interaction between the rare-earth layers, supporting the choice of AFM structure as a reference state for further calculations. Regarding the comparison with the experimental ground state, we use a collinear AFM configuration, because noncollinear magnetic states cannot be treated in the RSPt software (fully relativistic treatment is still included). However, this collinear approximation to the magnetic state is fairly reasonable, since in reality the degree of noncollinearity of these rare-earth systems is rather low. We model these systems by following the standard model for rare-earth compounds, i.e., that the $4f$ states of the rare-earth cations are considered as core states with zero dispersion and a fixed magnetic moment corresponding to Hund's rules in the atomic picture. These $4f$ core states affect the other electronic states, e.g., they spin-polarize the s , p , and d states of the same cations, which is relevant for determining the magnetic interactions (see further below). Importantly, the muffin-tin radius of the Ln cations is set as large as possible at 3.3 a.u., which affects the calculated muffin-tin magnetic moments and their interactions due to the spatial extent of the s , p , and d states mentioned before.

In (ii), strongly localized $4f$ electrons of the $LnRh_2Si_2$ compounds were treated as valence electrons and within the generalized gradient approximation (GGA) $+U$ approach [19]. The corresponding effective Hubbard parameter $U_{\text{eff}} = U - J = 6$ eV was chosen in such a way as to improve the agreement of calculated and experimental Néel temperatures T_N . The calculated T_N are shown in Appendix A.

Both methods (i) and (ii) provide similar electronic and magnetic structures of the compounds studied herein, as discussed in the following.

B. LKAG formula

We calculated the Heisenberg magnetic interactions between the rare-earth spins using the Liechtenstein-Katsnelson-

Antropov-Gubanov (LKAG) approach [20] (for a recent review, see [21]) using the full-potential linear muffin-tin orbital methods implemented in the RSPt software [15,16] as well as the fully relativistic Korringa-Kohn-Rostoker Green function method implemented in the code hutsepot [17,18]. The LKAG approach has an advantage compared to other methods in the literature, such as the total energy mapping, since it allows us to calculate interactions for distances of up to several lattice parameters without using excessively large supercells, which reduces the computational time significantly. It should be noted that, since we put the $4f$ states of the rare earth in the core in the RSPt calculations, the Heisenberg exchange is calculated including the s , p , and d states of the same cations, which are polarized due to large $4f$ moments. In the hutsepot calculations, the $4f$ states are treated as valence states using either GGA + U or self-interaction corrections (SICs), so the magnetic interactions between the rare-earth cations are calculated taking into account not only s , p , and d but also f states.

The magnetic energy of the system is described in this case by the classical Hamiltonian:

$$H = -\frac{1}{2} \sum_{j \neq i} J_{ij} \mathbf{e}_i \cdot \mathbf{e}_j. \quad (1)$$

Here, the unit vectors $\mathbf{e}_i = \mathbf{m}_i/m_i$ describe the direction of magnetic moment on each rare-earth cation at site i . Due to crystal symmetry, the Dzyaloshinskii-Moriya interactions in the studied systems are zero, thus they are not considered in the spin Hamiltonian (1). Also, we disregard relativistic corrections to the electronic structure when calculating the magnetic interactions in $LnRh_2Si_2$, but we discuss the effect of such corrections on the density of states in Sec. IV A. Importantly, we find that the calculated exchange parameters J_{ij} are quite sensitive to the calculation scheme. Both J_{ij} parameter sets (from RSPt and hutsepot) provide the correct magnetic ground state, but, since hutsepot values of the J_{ij} parameters provide better estimates of the magnetic ordering temperature, we use those values for the spin dynamics simulations in the two- and three-temperature model (see the next section).

III. ATOMISTIC MAGNETIZATION DYNAMICS AND TEMPERATURE MODEL

In atomistic spin dynamics simulations [22], the time evolution of atomic spins is governed by the Landau-Lifshitz-Gilbert equation [23,24], which can be expressed in Landau-Lifshitz form:

$$\frac{d\mathbf{m}_i}{dt} = -\frac{\gamma}{(1+\alpha^2)} \mathbf{m}_i \times (\mathbf{B}_i + \mathbf{B}_i^{\text{fl}}) - \frac{\gamma}{(1+\alpha^2)} \frac{\alpha}{m_i} \mathbf{m}_i \times (\mathbf{m}_i \times [\mathbf{B}_i + \mathbf{B}_i^{\text{fl}}]), \quad (2)$$

where \mathbf{m}_i is the magnetic moment of a given atomic site, unlike unit vectors \mathbf{e}_i that are used in Eq. (1), γ represents the gyromagnetic ratio, and α is the Gilbert damping. In contrast to the dynamics of $3d$ transition-metal systems, where the orbital angular momentum is quenched by the crystal field and electronic structure effects, the dynamics of rare-earth magnets is somewhat more complex. The reason is that the total angular momentum from spin and orbital moments must

enter the time evolution of the moment, according to Eq. (2). In Russel-Saunders coupling, the strong spin-orbit interaction of the $4f$ shell couples the total spin (S) and orbital (L) angular momentum to a common angular momentum J , whose contribution to the magnetic moment of the $4f$ shell is provided by $g_J J$, where g_J is the Landé g -factor. Although the orbital moment is then dynamically active in the actual simulations of the magnetism provided by J , the torque that propels the dynamics, via the effective field, \mathbf{B}_i in Eq. (2), is normally assumed to be given by spin-only contributions to the exchange interaction in Eq. (1). It should be noted that expressions for the orbital contribution to exchange interactions have been published [25], but they are for most systems assumed to be vanishingly small. We have indeed made this assumption in the present work. The spin-driven exchange field, $\mathbf{B}_i = -\partial H/\partial \mathbf{m}_i$, in this work is therefore obtained from the spin Hamiltonian, Eq. (1), where the exchange parameters J_{ij} are obtained from the hutsepot code. In our simulations, temperature is included by means of Langevin dynamics where we introduce a stochastic field \mathbf{B}_i^{fl} as white noise with properties $\langle B_{i,\mu}^{\text{fl}}(t) B_{j,\nu}^{\text{fl}}(t') \rangle = 2D_i^M \delta_{ij} \delta_{\mu\nu} \delta(t-t')$ with $\mu, \nu = x, y, z$. In particular, in these calculations we employ $D_i^M = \alpha k_B T_e / (1 + \alpha^2) \gamma m_i$, where T_e and k_B are the electronic temperature and Boltzmann constant, respectively (see Ref. [26]). The formalism above is available in the UppASD [26] code, which was used for all simulations in this work. In our simulations of ultrafast demagnetization dynamics, we employ simulation cells with a $40 \times 40 \times 40$ repetition of the unit cell, using periodic boundary conditions. In addition, $N_t = 10^6$ time steps of $dt = 10^{-16}$ s were used. In this work, we reduce the HC3TM to calculate electron and spin temperatures in ultrafast magnetization dynamics simulations. We choose to exclude the lattice temperature from consideration since it is stated in Ref. [10] that materials under investigation here have very similar $4f$ spin arrangement, crystal structure, and chemical bonding characteristics with only a 2.5% difference in lattice constants. It should be noted that the only difference between them is the occupation of the localized $4f$ shell of the Ln ions, and hence the magnetic moment. Therefore, it is reasonable to study whether the difference between the studied systems is only due to the exchange interactions, and whether it is sufficient to reproduce experimental findings without taking the lattice part into account. We attempt to answer this question in the present work.

In this work we primarily use the HC2TM (see Fig. 1), with only spin and electron temperatures considered, but we make a detailed comparison between HC2TM and HC3TM for one of the compounds considered here. In the HC2TM, we modify the expression for the time-dependent electronic temperature dynamics in the HC3TM, proposed in Refs. [2,7], to study a case of a fixed lattice temperature, and we obtain

$$\Delta T_e(t) = -\frac{C_s(T_s)}{C_e(T_e)} \Delta T_s(t) + \frac{W(t)}{C_e(T_e)} \Delta t - \frac{G_{\text{cool}}(T_e - T_{\text{final}})}{C_e(T_e)} \Delta t. \quad (3)$$

Here, the spin temperature is defined by the expression $T_s = \frac{m(\sum_i |\mathbf{m}_i \times \mathbf{B}_i|^2)}{2k_B(\sum_i \mathbf{m}_i \cdot \mathbf{B}_i)}$, where \mathbf{e}_i is the normalized local spin moment [27]. The details of calculating spin and electronic

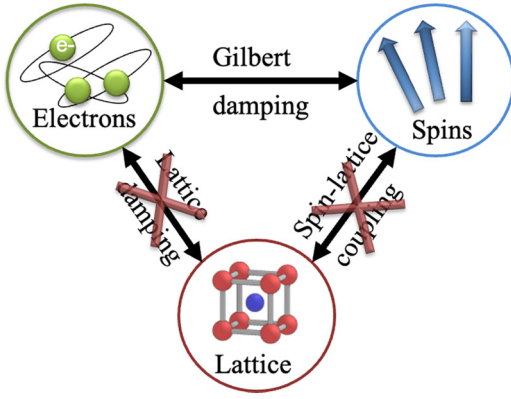


FIG. 1. Schematic of the HC2TM model.

temperatures in HC3TM can be found in Ref. [7]. Also, $C_e(t)$ and $C_s(t)$ are electron and spin heat capacities, respectively. The electronic heat capacities are obtained from the Sommerfeld model (see Appendix A), and temperature-dependent spin heat capacities are calculated using, as shown in Sec. IV C, exchange constants described in Sec. IV B. The laser impact is captured by the term $W(t) = P_0 \exp(-(t - t_0)^2/2\sigma^2)$ which is modeled as a Gaussian, where t_0 is the center of the pulse, P_0 represents the absorbed pump pulse power amplitude (per area), $\sigma = 0.02$ ps is the pulse width, and Δt is a time step.

G_{cool} corresponds to heat dissipation from the laser-affected spot to the whole sample. This term is relevant in this study because of the rather big timescales of demagnetization (up to 400 ps for holmium). Moreover, this term can serve as an additional cooling channel partly substituting a full treatment of the lattice subsystem. Here, we choose the value of G_{cool} so the remagnetization is close to the experimentally observed one. The value of $G_{\text{cool}} = 3 \times 10^{14}$ J/s is similar for all materials studied here.

In addition to HC2TM described above, for one of the compounds (GdRh_2Si_2) we utilize HC3TM [2,7] to quantify the impact of lattice dynamics on ultrafast demagnetization. To do this, we perform coupled atomistic spin-lattice dynamics simulations, described by Eqs. (2), (C1), and (C2), with lattice parameters described in Appendixes B and C. In HC3TM, to calculate electron temperature T_e , we add to the right side of Eq. (3) the following term:

$$-\frac{C_l(T_l)}{C_e(T_e)} \Delta T_l(t), \quad (4)$$

where the lattice temperature is calculated from the kinetic energy $\langle E_l^{\text{kin}} \rangle / k_B$. Kinetic energies E_l^{kin} are extracted from coupled spin-lattice dynamics simulations, with equations governing lattice dynamics described in Appendix C. Spin temperatures and heat capacities are calculated in the same way as in HC2TM (see Fig. 1).

IV. RESULTS

A. Electronic structure

The electronic structure of LnRh_2Si_2 was examined by both scalar- and fully relativistic approaches. Although $4f$ elements were treated as core electrons in our scalar-relativistic

RSPt calculations, the densities of states (DOSs) at the Fermi level are very similar in both approaches (see Fig. 2). This is crucial for the Ruderman-Kittel-Kasuya-Yosida (RKKY) interaction, which is a dominant interaction between the localized $4f$ magnetic moments in these systems. However, the DOSs in the range of the valence bands are different in both approaches in the case where the total angular moment of the $4f$ atom is larger than zero. The most prominent deviations occur for Dy and Ho cases, since the spin-orbital interaction and other relativistic effects are significant in these systems. However, since $4f$ states continue to be sufficiently localized, their positions do not affect the DOS at the Fermi level, which is mainly of $5d$ character. Nevertheless, the position of $4f$ states can be important for other types of interaction between the magnetic moments, for example the indirect double exchange interaction via Si sp states. Thus, although treating $4f$ states as core might predict correctly the ground state, since the RKKY interaction is dominant in these systems, the critical temperature might be estimated wrongly by this approach.

The obtained magnetic moments are presented in Table I. In the scalar-relativistic calculations, the spin moment of the $4f$ states is fixed at the value obtained from the Russell-Saunders rules, while the contribution from the s -, p -, and d -states is calculated self-consistently using DFT. This spd -contribution is similar both in scalar- and fully relativistic calculations for some of the compounds (e.g., Tb-, Ho-, and Pr-based), but it can be visibly different for others (e.g., Gd and Dy cases), as one can see from the middle column of Table I. Relativistic calculations with $4f$ electrons in the valence parts provide also orbital moments, which are substantial for all elements except for Gd. Nevertheless, the magnitude of the DOS at the Fermi level is almost the same in both approaches. This is crucial for the RKKY interaction, which is dominant in this family of LnRh_2Si_2 compounds. Therefore, both scalar- and fully relativistic methods should deliver a similar behavior for Heisenberg exchange constants, which are discussed in the next subsection. We note that the deviations of the spd -moments can partly explain the quantitative differences in the Heisenberg interactions that we obtain using the two calculation methods.

The layered crystal structure of LnRh_2Si_2 is schematically presented in Fig. 2 with crystal structure parameters, demonstrating very close values of lattice parameters, given in Appendix D.

B. Exchange coupling constants

The Heisenberg exchange parameters calculated using the RSPt code for LnRh_2Si_2 show certain characteristic trends. In particular, the interlayer exchange J_3 which stabilizes the AFM-coupled rare-earth layers scales mostly linearly with the de Gennes factor (see the supplementary material for Ref. [10]). The largest deviations from linearity are observed for $\text{Ln} = \text{Pr}$ and Tb. This linear trend is also discussed in previous work [10], where the magnetic interactions were calculated using both LMTO and KKR methods, and the latter show a similar but more linear trend. Overall, these results suggest a physical picture where the magnetic exchange between the rare-earth moments is mediated by conduction

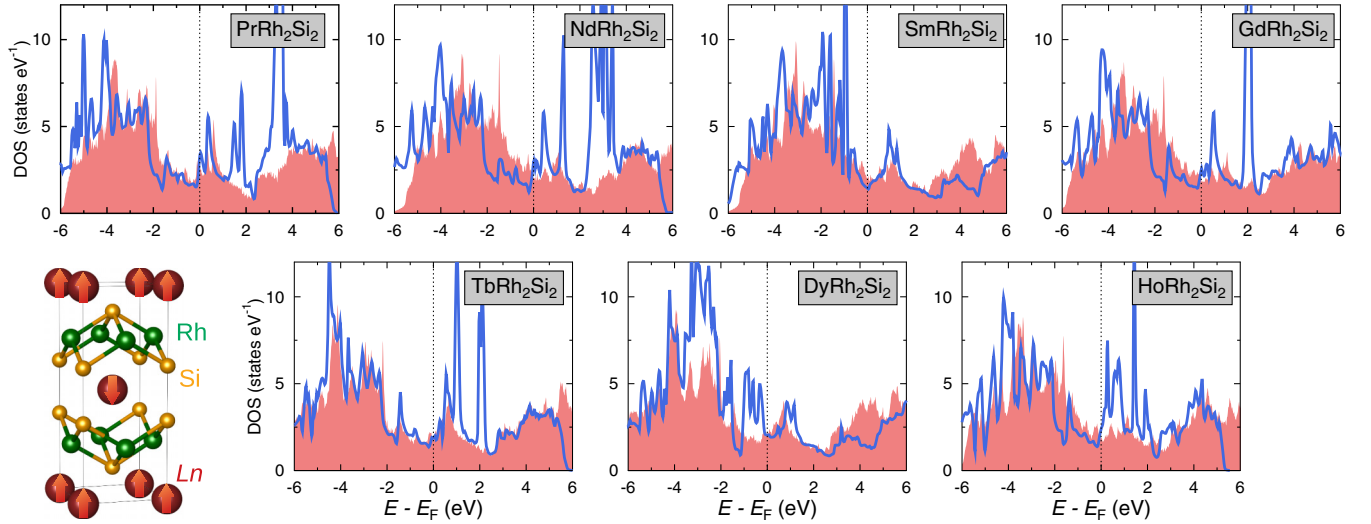


FIG. 2. Density of states calculated for the antiferromagnetic state of different rare-earth compounds $LnRh_2Si_2$ ($Ln = Pr, Nd, Sm, Gd, Tb, Dy, Ho$) using scalar relativistic $4f$ in the core (red filling) and the fully relativistic GGA + U method (blue lines), and a schematic of the layered crystal structure with the direction of Ln moments.

electrons, leading to RKKY-like character of interactions (see Appendix F) and linear scaling with the de Gennes factor, already discussed in depth in Ref. [10].

C. Magnetic ground state

Following the experimental studies of Ref. [10], we start the analysis of the magnetic properties of the system by performing calculations of the temperature dependence of the magnetization using the calculated exchange constants discussed above. The results of these calculations are presented in Fig. 3, where the average magnetization curves for one of the AFM sublattices are shown. It can be seen from the figure that, despite very different magnetic moments and Néel temperatures, the normalized magnetization as a function of normalized temperature behaves similarly for all studied materials, in agreement with experimental observations [10]. In addition, in Fig. 4 we also present the heat capacities of the spin system, which will be further used for calculations of ultrafast demagnetization dynamics in HC2TM in particular as an input into Eq. (3). Spin heat capacities have not been

reported for these systems in the literature so far, to the best of our knowledge. In general, the importance of taking into account temperature-dependent heat capacities in HC3TM was discussed in Ref. [2]. In calculations of spin heat capacities, we employ the widely used classical approach based on Boltzmann statistics (see Refs. [2,28] and references therein).

D. Ultrafast demagnetization

To get a deeper understanding of the ultrafast demagnetization in $LnRh_2Si_2$, we performed atomistic spin dynamics simulations starting from temperature 50 K. In the spin dynamics simulations, we used the same value of the Gilbert damping for all materials. The value of the Gilbert damping was chosen to be 0.001 (see [29]), which is a realistic value for antiferromagnets, and with this choice one obtains simulated magnetization curves that are close to experimentally observed values. We use the same Gilbert damping α value for all materials, because it was shown in Ref. [10] that Gilbert damping does not scale with the de Gennes factor, and it is expected that the valence-band electronic structure is similar

TABLE I. Calculated magnetic m^s and orbital moments m^l of the rare-earth Ln cations in $LnRh_2Si_2$ compounds. The left and right parts of the middle columns show the results where the $4f$ states of Ln cations are set as the core states (“core”) and from fully relativistic GGA+ U method. The de Gennes factor $G = (g - 1)^2 J(J + 1)$ together with the interlayer Heisenberg exchange J_3 calculated from hufsetop (second to last column) and RSPt (last column) are indicated as well.

Ln	$m_{4f}^s (\mu_B)$		$m_{spd}^s (\mu_B)$		$m_f^l (\mu_B)$	G	$J_3 (\mu Ry)$	$J_3 (\mu Ry)$
	Core	GGA + U	Core	GGA + U	GGA + U		GGA + U	Core
Pr	1.60	0.63	0.07	0.06	3.25	0.80	-5.6	-5.5
Nd	2.45	2.54	0.08	0.14	5.81	1.84	-4.1	-5.3
Sm	3.43	2.88	0.10	0.08	1.52	4.11	-6.0	-8.1
Gd	7.00	7.03	0.18	0.30	0.00	15.8	-15.7	-23.7
Tb	6.00	5.58	0.19	0.22	2.27	10.5	-10.8	-31.4
Dy	5.00	3.63	0.15	0.09	6.02	7.08	-6.8	-12.9
Ho	4.00	3.24	0.11	0.12	5.42	4.50	-6.7	-5.0

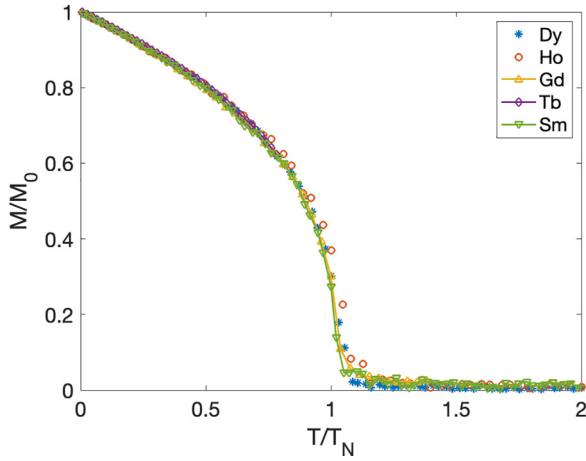


FIG. 3. Normalized magnetization M/M_0 as a function of normalized temperature for $LnRh_2Si_2$ materials with different Ln elements specified in the figure legend.

for all systems investigated here, as Fig. 2 also confirms. It should be noted that we have in fact studied the influence of Gilbert damping values in the range 0.001–0.05, and we can confirm that in this range, the choice of Gilbert damping does not change the main conclusions presented in this work. We note, however, that while for Tb-, Gd-, and Ho-based AFM this Gilbert damping provides realistic demagnetization times, for Sm it results in much slower demagnetization, which was observed in the experiment. To obtain faster demagnetization, higher Gilbert damping, or taking into account the lattice, might be necessary. However, as stated above, this does not change the main conclusions of the paper. Typical spin and electron temperatures from our simulations are presented in Fig. 5 for $TbRh_2Si_2$. The lattice temperature remained fixed during our simulations (data not shown), as discussed above. The qualitative comparison of obtained spin and electronic temperatures with ones reported using HC3TM in [2,7] shows similarities in behavior, such as rapid growth of electronic

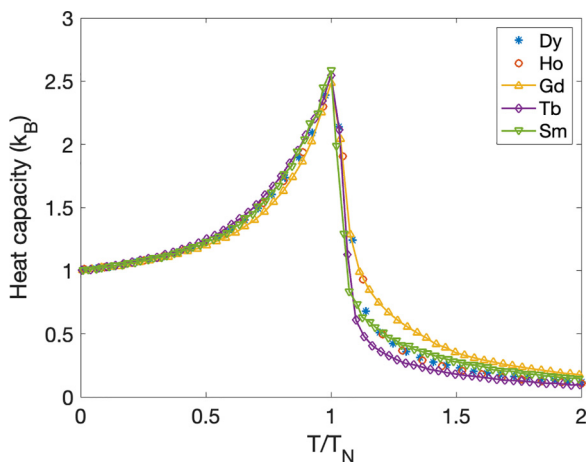


FIG. 4. Temperature-dependent spin heat capacities for $LnRh_2Si_2$ materials with different Ln cations specified in the figure legend. The temperatures are normalized to the corresponding Néel temperatures T_N .

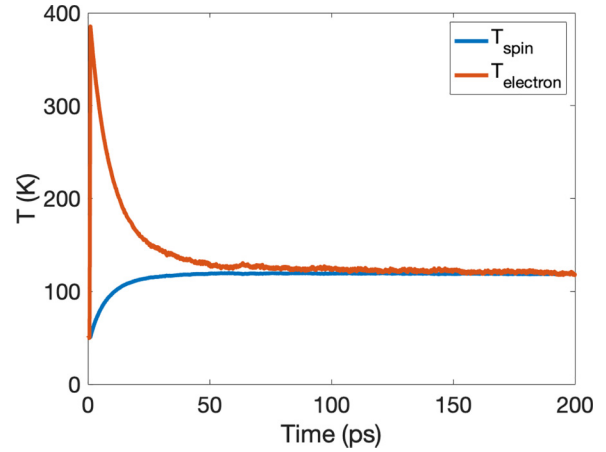


FIG. 5. Temperature dynamics of $TbRh_2Si_2$ for a laser fluence $2.34 J/m^2$, $\alpha = 0.001$.

temperature following the absorption of the pulse, and then slower growth of spin temperature. Based on how effective temperature models are constructed, disregarding the lattice subsystem should have a similar effect to increasing the laser pulse or, alternatively, to a case of vanishing lattice damping. Additional tests (data not shown) on fcc Ni confirm this behavior. The other features of the magnetization curve remain the same. We show in Sec. IV E that HC2TM is able to reproduce the main features of system dynamics, even if the changes of the lattice temperature are disregarded.

Calculated ultrafast magnetization dynamics curves of $TbRh_2Si_2$ are shown in Fig. 6(a) for several values of laser fluence.

It can be seen from Fig. 6(a) that the demagnetization process consists of two main parts. It begins with a fast magnetization drop (marked by a red shaded area), followed by a second slower decay (shown by a green shaded area). This two-step behavior was confirmed by fitting the obtained

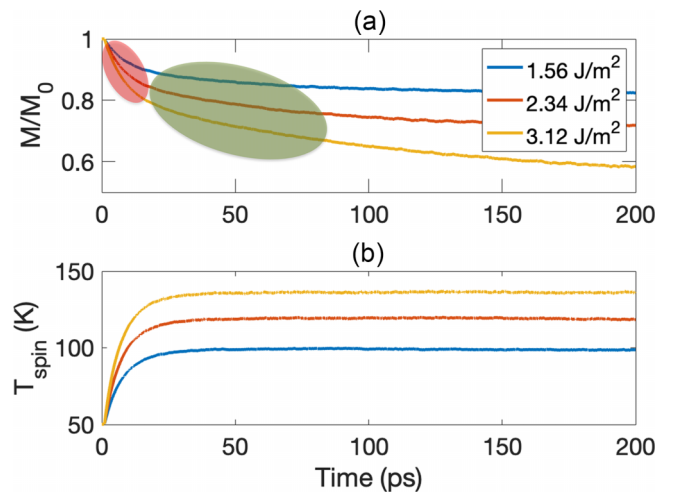


FIG. 6. Magnetization dynamics (a) and spin temperature dynamics (b) of $TbRh_2Si_2$ for various laser fluences. Shaded areas indicate fast (red) and slow (green) parts of the demagnetization process.

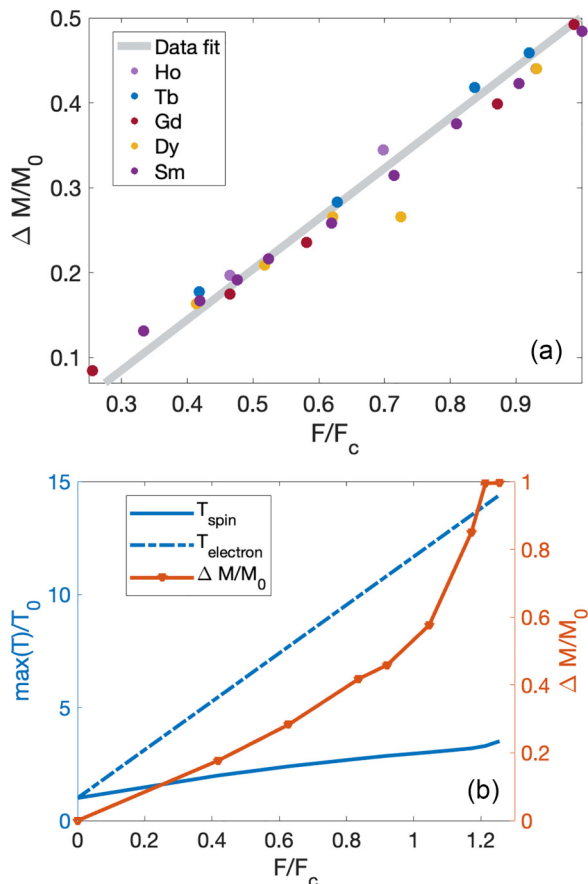


FIG. 7. (a) Total demagnetization amplitude as a function of normalized laser fluence. The line is a guide for the eye. (b) Normalized spin and electron temperatures and total demagnetization amplitude as a function of a normalized laser fluence for TbRh_2Si_2 .

magnetization curves with exponential functions, following the experimental study in Ref. [10], as shown in Appendix A. In addition, as the figure shows, the first part of the demagnetization process becomes faster for higher laser fluence, which is in agreement with experimental observations [10]. The other studied materials exhibit similar behavior: first fast demagnetization, followed by slower demagnetization. In addition, we present the dynamics of spin temperatures for various fluences shown in Fig. 6(b), which demonstrates the same trend as magnetization dynamics, specifically the first sharp rise of the spin temperatures, which is followed by a slower increase and thermalization.

Next, we investigate the impact of laser fluence on the total demagnetization amplitude for all materials. Since the considered materials have a big difference in T_N , and, therefore, required different fluences for demagnetization, we adopt the concept of a critical laser fluence F_c from Ref. [10], which is the laser fluence leading to demagnetization amplitude $\Delta M/M_0 = 0.5$ (for example, 3.73 J/m^2 is the F_c for TbRh_2Si_2). The total demagnetization amplitude for all materials as a function of normalized fluence (i.e., laser fluence divided by the critical laser fluence) is presented in Fig. 7(a), and this is the main result of the present study. It can be seen from Fig. 7(a) that the results of our simulations agree in general with experimental observations [see Fig. 2(d) in

Ref. [10]], where a linear relationship between $\Delta M/M_0$ and normalized fluence was observed for this set of systems.

In the experimental data of Ref. [10] for higher fluences $F/F_c > 1$ or/and demagnetization amplitudes $\Delta M/M_0 > 0.5$, the experimental results start to deviate from linear dependence [see Fig. 2(d) of Ref. [10]], especially for the Tb-system. We observe a similar deviation from linear behavior for $F/F_c > 1$ in our simulations, as shown for Tb in Fig. 7(b). Similar behavior with fluence higher than critical is observed across all materials studied herein (data not shown).

To further analyze this nonlinear behavior, we performed simulations for higher fluences than those used in the experiments of Ref. [10]. The results of these simulations are shown in Fig. 7(b), where we focus on the electron and spin temperature as well as $\Delta M/M_0$. It can be seen from Fig. 7(b) that while electronic and spin temperatures increase linearly with laser fluence for all fluences used in the simulations, the demagnetization amplitude demonstrates a linear behavior only for smaller fluences F . In particular, for $F > F_c$ the deviation from a linear behavior of $\Delta M/M_0$ is quite noticeable. It can be seen from Fig. 7(b) that the temperatures calculated in the magnetization dynamics simulations behave linearly with fluence, therefore it is possible to relate fluence in ultrafast demagnetization simulations to the temperature. Then, the demagnetization amplitude $\Delta M/M_0$ extracted from ultrafast demagnetization curves at various fluences can be compared to a transient M/M_0 curve versus temperature (and not fluence) that has the same shape as the static curve shown in Fig. 3. Hence, we find that the transient $\Delta M/M_0$ curve of Fig. 7(b) has strong similarities with the static $M(T)$ curve presented in Fig. 3, which suggests that the out-of-equilibrium magnetization of the presently studied materials simply follows a static $M(T)$ curve at low fluences. Over the picosecond timescales that are relevant for the dynamics of this class of materials, the simulations suggest that a quasiequilibrium is reached for the distribution of atomic moments, and this quasiequilibrium evolves in time following the electronic temperature obtained in the simulations.

E. Comparing the HC2TM and HC3TM for GdRh_2Si_2

To investigate the importance of lattice dynamics for the ultrafast demagnetization, we perform coupled atomistic spin-lattice dynamics simulations of GdRh_2Si_2 , and we apply the heat-conserving three-temperature model (HC3TM), which was proposed and described in detail in Refs. [2,7]. In these simulations, we do not include spin-lattice coupling specifically in the Hamiltonian. Instead, coupling between spin and lattice subsystems takes place as a flow of heat between the two systems, in part mediated by the electron temperature (for details, see Refs. [2,7]). It was shown in Ref. [7] that even in the absence of explicit spin-lattice coupling in the Hamiltonian (e.g., as introduced in Ref. [30]), lattice dynamics can play an important role in ultrafast demagnetization, impacting demagnetization amplitude and remagnetization. Details of lattice dynamics simulations, needed for the HC3TM, are presented in Appendix B. This includes the equations of motion, lattice damping, and calculations of the force constant. In these simulations, the spin-dynamics is treated according to Eqs. (1) and (2).

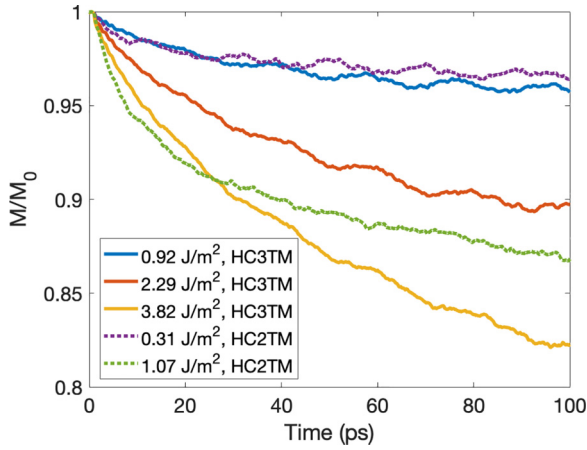


FIG. 8. Magnetization dynamics of GdRh_2Si_2 in HC3TM (solid lines) and HC2TM (dashed lines) for various laser fluences.

We start by studying ultrafast magnetization dynamics for various fluences, and we compare the results of HC3TM with HC2TM for GdRh_2Si_2 . It can be seen from Fig. 8 that an account of lattice dynamics, as provided in the HC3TM, leads to slower magnetization dynamics especially during the first 10–20 ps. Moreover, while comparing HC2TM and HC3TM for the same (or similar) fluence, we observe that HC2TM leads to higher demagnetization amplitude. Interestingly, a very similar demagnetization rate during the first 10–20 ps is observed for the HC2TM and HC3TM, provided one considers different fluences. For instance, the 1.07 J/m^2 HC2TM data are almost on top of the 3.82 J/m^2 HC3TM data, and the 0.31 J/m^2 HC2TM data lie almost on top of the 0.92 J/m^2 HC3TM data. Hence, for the present system it seems that a scaling of fluence with a factor 3–4 provides very similar results for simulations of HC2TM and HC3TM. In general, the magnetization curves in both models lead to similar features of the magnetization dynamics, such as faster magnetization drop and then slower demagnetization on longer timescales, which justify the use of HC2TM and the results provided in Fig. 7. The typical example of temperature dynamics for HC3TM can be found in Appendix E.

The transfer of heat between electrons and lattice is tuned by several interactions, one being the lattice damping ν parameter (see Appendix for details and Refs. [2,7]). It can be seen in Fig. 9(b) that a smaller lattice damping leads to faster demagnetization and slightly larger demagnetization amplitude, which is consistent with previous results for $3d$ ferromagnets [7]. This trend also explains faster demagnetization and bigger demagnetization amplitudes in HC2TM, compared to HC3TM, which can be considered as a limit of zero lattice damping as shown in Fig. 9(b). Increase of demagnetization amplitude with reduction in lattice damping is connected to a higher amount of heat transferred from electrons to the spin system and, therefore, the higher spin temperatures, as can be seen at Fig. 9(b).

We complete our analysis of how the lattice dynamics impact the magnetization dynamics by considering the demagnetization amplitude as a function of normalized laser fluence in the HC3TM and comparing it with values obtained in HC2TM. This is presented in Fig. 10. We would like to

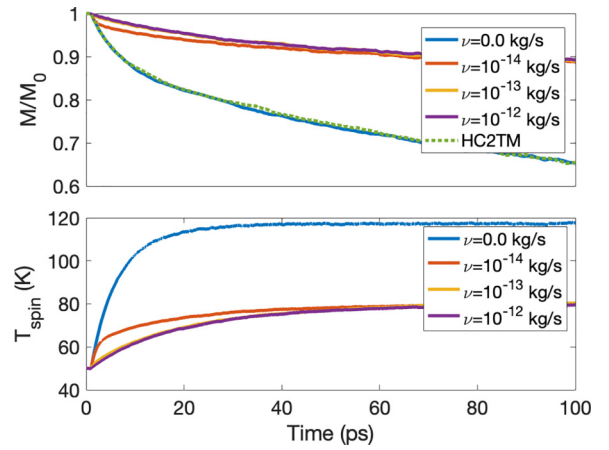


FIG. 9. (Top panel) Magnetization dynamics of GdRh_2Si_2 in HC3TM (solid lines) for various values of lattice damping (laser fluence 2.29 J/m^2) in comparison with magnetization dynamics of GdRh_2Si_2 in HC2TM (dashed lines). (Bottom panel) Corresponding spin temperature dynamics for various values of lattice damping (laser fluence 2.29 J/m^2).

note that F_c for GdRh_2Si_2 is different in HC3TM and HC2TM, due to the differences in the simulations, as discussed above. Taking this difference into account, it can be seen from Fig. 10 that HC2TM and HC3TM lead to a very similar linear relationship between magnetization amplitude and normalised fluence. As can be seen, details of the lattice dynamics do not impact this linear trend at low fluences, confirming the suitability of HC2TM for studying ultrafast demagnetisation dynamics in the present system and for validation of the results shown in Fig. 7.

V. CONCLUSIONS

In this work, we give a thorough account of the theoretical results of the electronic and magnetic properties of the LnRh_2Si_2 system, based on DFT coupled to a method for evaluating spin Hamiltonian parameters [20,21]. From the spin Hamiltonian, an effective Weiss field can be calculated that is used here in atomistic spin-dynamics simulations

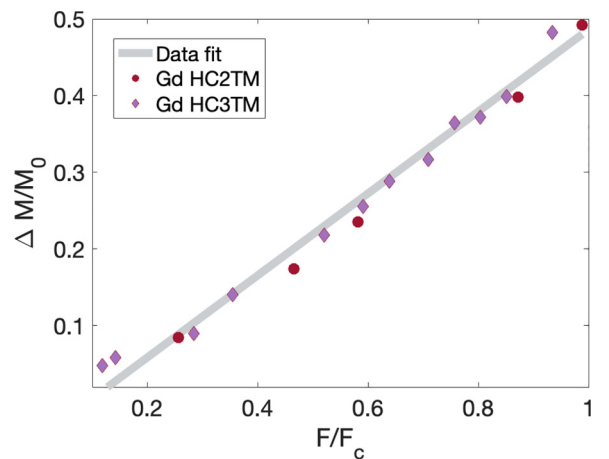


FIG. 10. Total demagnetization amplitude in HC2TM (red circles) and HC3TM (violet diamonds) for GdRh_2Si_2 .

[26] coupled to a heat-conserving temperature model [2] that enables calculations of transient temperature profiles relevant for simulations of pump-probe experiments.

The simulations presented here for $LnRh_2Si_2$ agree with experimental observations of pump-probe experiments, especially for lower fluences, where in Ref. [10] the demagnetization amplitude as a function of fluence was studied for amplitudes smaller than $F/F_c = 0.5$. Similar linear dependencies of demagnetization amplitude on laser fluence are widely reported for various materials both from theoretical and experimental studies [7,10,11,31,32], however the motivation behind this linear trend has only been discussed infrequently and therefore it remains poorly understood. It was reported in Ref. [7] (see Fig. 4 in the Supplementary Information of that paper) that for elemental ferromagnets, the spin temperature and transient magnetization during the ultrafast magnetization dynamics deviate very little from the equilibrium $M(T)$ curve. Our findings here for antiferromagnetic compounds are consistent with the observations of Ref. [7]. Hence a picture that emanates from these works, as well as of Ref. [33], is that the transient magnetization can be described as resulting from a quasiequilibrium distribution of the atomic moments, and that this distribution evolves in time as a result of the changes of the temperature. It should be noted here that it is primarily for these simulations that the electronic temperature is relevant, since in heat-conserving temperature models for transient magnetism the electronic temperature enters the fluctuating field that changes the magnetic state.

Finally, we note that from the simulations put forth here, one predicts that for higher fluences the demagnetization amplitude starts to deviate from linearity; for values of $F/F_c > 1.0$, a superlinear behavior is quite distinct. It was shown that this result does not depend on accounting for or disregarding lattice dynamics in simulations.

ACKNOWLEDGMENTS

This work was financially supported by the Knut and Alice Wallenberg Foundation through Grants No. 2018.0060, No. 2021.0246, and No. 2022.0108. O.E. and M.P. acknowledge support from the Wallenberg Initiative Materials Science for Sustainability (WISE) funded by the Knut and Alice Wallenberg Foundation (KAW). O.E. also acknowledges financial support from the Swedish Research Council (Vetenskapsrådet, VR), the European Research Council (854843-FASTCORR), and STandUP. M.P. acknowledge support from Olle Engkvist Foundation (Grant No. 218-0077) and from WISE-WASP joint call. O.E. and A.B. acknowledge eSENCE for financial support. A.B. acknowledges the Carl Trygger Foundation (CTS) and Uppsala University's AI4Research for financial support. D.T. acknowledges financial support from the Swedish Research Council (Vetenskapsrådet, VR) Grants No. 2019-03666 and No. 2023-04239. A.E. acknowledges the funding by the Fonds zur Förderung der Wissenschaftlichen Forschung (FWF) under Grant No. I 5384. L.R. and Y.W.W. acknowledge funding from the Deutsche Forschungsgemeinschaft (DFG, German Research Foundation) within the Transregio TRR 227 - 328545488 Ultrafast Spin Dynamics (Projects No. A10 and B07). This publication is part of the project NL-ECO: Netherlands Ini-

TABLE II. Calculated (using hutsepot and RSPt codes) and experimental [10] Néel temperatures.

Ln	Ho	Dy	Nd	Sm	Pr	Tb	Gd
T_N (K), Hutsepot	61	91	76	91	100	151	131
T_N (K), RSPt	<10	39	18	<10	12	72	20
T_N (K), exp.	27	52-55	53	64	68	94	106

tiative for Energy-Efficient Computing (with project number NWA. 1389.20.140) of the NWA research programme Research Along Routes by Consortia, which is financed by the Dutch Research Council (NWO). The computations were enabled by resources provided by the National Academic Infrastructure for Supercomputing in Sweden (NAISS) at the National Supercomputing Centre (NSC, Tetralith cluster) partially funded by the Swedish Research Council through Grant Agreement No. 2022-06725. The structural sketch in Fig. 2 was produced using the VESTA3 software [34].

DATA AVAILABILITY

The data that support the findings of this article are not publicly available. The data are available from the authors upon reasonable request.

APPENDIX A: DETAILS OF SPIN AND SPIN-LATTICE DYNAMICS CALCULATIONS

To apply HC3TM and HC2TM, in Eqs. (3) and (4) spin heat capacities were calculated as described in Sec. IV C, with the Néel temperatures of all compounds extracted from the spin heat capacities, which are summarized in Table II and compared with the measured quantities.

The electronic heat capacities used in simulations are obtained from the Sommerfeld model $C_e(T) = \gamma T$. For $GdRh_2Si_2$, $\gamma = 6 \text{ mJ mol}^{-1} \text{ K}^{-1}$ is used, which is in the range reported in [12,35]. For other compounds, $\gamma = 7 \text{ mJ mol}^{-1} \text{ K}^{-1}$ is used, except Sm. To test the impact of electronic heat capacities on the main conclusions of our paper, for $SmRh_2Si_2$ we have performed calculations both for $\gamma = 7$ and $13 \text{ mJ mol}^{-1} \text{ K}^{-1}$, which does not change the main conclusions of the paper (the linear dependence of demagnetization amplitude on laser fluence). The only difference between two electronic heat capacities studied is a slightly faster demagnetization rate for subpicosecond timescales, and a bit higher demagnetization amplitude. Even for almost twice higher γ , the difference between the demagnetization

TABLE III. Coefficients for the fitting of M_1/M_0 and M_2/M_0 functions.

Coeff.	d_{fast}	d_{slow}	τ_{slow}	τ_{fast}
Gd				
M_1/M_0	0.1045	0.3199	80.09	6.198
M_2/M_0		0.3862	44.79	
Tb				
M_1/M_0	0.1927	0.3133	102.3	8.202
M_2/M_0		0.4332	35.29	

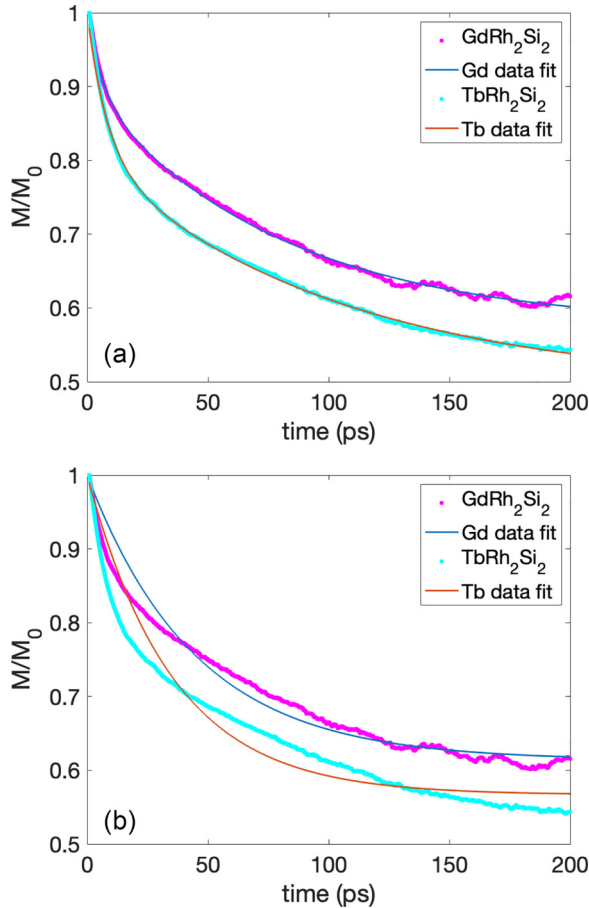


FIG. 11. Magnetization dynamics of GdRh₂Si₂ (HC3TM) and TbRh₂Si₂ (HC2TM) and the fit with (a) $M_1(t)/M_0$ and (b) $M_2(t)/M_0$.

amplitude is around 15% in the studied temperature range, and it does not affect the behavior with fluence, which is one of the main results reported in the paper.

The lattice heat capacity C_l for GdRh₂Si₃ HC3TM simulations is calculated from the Debye model with a Debye temperature $T_D = 148$ K reported in [35].

To confirm the two-step behavior of demagnetization in our simulations, we followed the experimental paper [10], where the same compounds were studied experimentally, and the two-step demagnetization was observed for all compounds. Specifically, the magnetization curves were fitted to the same equation in the form

$$M_1(t)/M_0 = 1 - \theta(t)(d_{\text{fast}}[1 - \exp(-t/\tau_{\text{fast}})] + d_{\text{slow}}[1 - \exp(-t/\tau_{\text{slow}})]),$$

where $\theta(t)$ is a Heaviside function. Magnetization reduction from two processes is denoted d_{fast} and d_{slow} with corresponding demagnetization times $\tau_{\text{fast/slow}}$.

To compare with the case of only one exponent, we fitted the same magnetization curves to the function

$$M_2(t)/M_0 = 1 - \theta(t)(d[1 - \exp(-t/\tau)]).$$

The results of the fitting of magnetization dynamics with functions $M_1(t)/M_0$ and $M_2(t)/M_0$ are presented in Fig. 11 for Tb- and Gd-based compounds. It can be seen from Fig. 11 that the

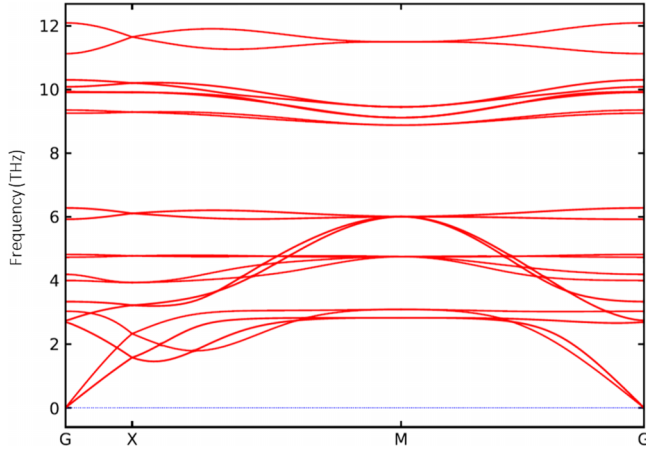
TABLE IV. Force constant matrix elements for each pair $i-j$ in the two-formula-unit cell.

Pair $i-j$	Φ_{xx}	Φ_{xy}	Φ_{xz}
	Φ_{yx}	Φ_{yy}	Φ_{yz}
	Φ_{zx}	Φ_{zy}	Φ_{zz}
1-1	5.17472	0.00000	0.00000
	0.00000	5.17472	0.00000
	0.00000	0.00000	6.26490
1-2	0.01013	0.00000	0.00000
	0.00000	0.01013	0.00000
	0.00000	0.00000	0.28652
1-3	0.21722	0.00000	0.00000
	0.00000	-0.59987	0.00000
	0.00000	0.00000	-0.97715
1-4	0.21722	0.00000	0.00000
	0.00000	-0.59987	0.00000
	0.00000	0.00000	-0.97715
1-5	-0.59987	0.00000	0.00000
	0.00000	0.21722	0.00000
	0.00000	0.00000	-0.97715
1-6	-0.59987	0.00000	0.00000
	0.00000	0.21722	0.00000
	0.00000	0.00000	-0.97715
1-7	-0.35841	0.00000	0.00000
	0.00000	-0.35841	0.00000
	0.00000	0.00000	-0.91007
1-8	-0.35841	0.00000	0.00000
	0.00000	-0.35841	0.00000
	0.00000	0.00000	-0.91007
1-9	-1.84982	0.00000	0.00000
	0.00000	-1.84982	0.00000
	0.00000	0.00000	-0.41154
1-10	-1.84982	0.00000	0.00000
	0.00000	-1.84982	0.00000
	0.00000	0.00000	-0.41154

function $M_1(t)/M_0$ provides a better fitting of magnetization dynamics for both compounds. The values of fitting coefficients τ , $\tau_{\text{fast/slow}}$, and d , $d_{\text{fast/slow}}$ for the curves in Fig. 11 are given in Table III.

APPENDIX B: FORCE CONSTANTS CALCULATION

We used the Vienna Ab-initio Simulation Package (vasp) [36] and phonopy [37] to compute the force constants required for spin-lattice dynamics simulations. First, we used a two-formula-unit tetragonal unit cell to perform DFT calculations using the projected augmented wave (PAW) method [38], as implemented in vasp [36]. The exchange-correlation functional was described using the generalized gradient approximation (GGA) with the Perdew-Burke-Ernzerhof (PBE) parametrization [39]. A plane-wave energy cutoff of 500 eV was applied for the basis set, along with a Γ -centered Monkhorst-Pack k -mesh of $20 \times 20 \times 10$ to ensure convergence of the total energy and local magnetic moments. To accurately capture the localized nature of Gd $4f$ electrons, we employed DFT + U calculations using the Hartree-Fock approximation [40]. The rotationally invariant formulation by Liechtenstein *et al.* [41] was applied with Coulomb

FIG. 12. Phonon band structure of GdRh₂Si₂.

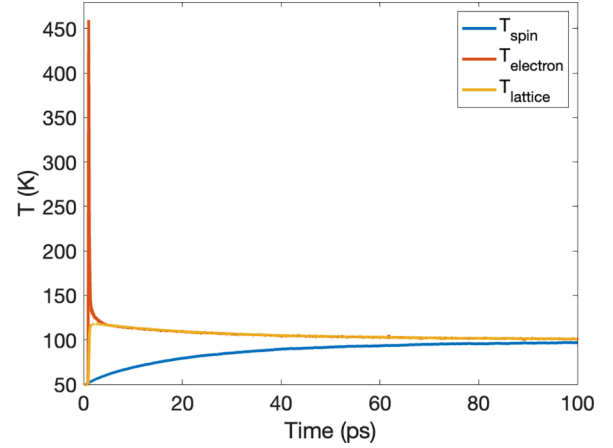
interaction parameters $U = 6.7$ eV and $J = 0.7$ eV for the Gd $4f$ states, based on prior studies [42]. Before calculating the force constants, the experimental unit cell [10] was fully relaxed, optimizing atomic positions, cell shape, and volume to meet a force convergence criterion of 1 meV/Å. Force constants for the relaxed structure were computed using phonopy [37] and density functional perturbation theory (DFPT), as implemented in vasp [36]. The force constant matrix elements (eV/Å²) are tabulated in Table IV, with Gd at position (0, 0, 0) in the two-formula-unit tetragonal cell containing 10 atoms taken as the reference. The atomic positions of Gd, Rh, and Si in the two-formula-unit tetragonal cell are as follows. The cell contains two Gd atoms, four Rh atoms, and four Si atoms. The positions are given in direct coordinates:

Gd: (0.00000, 0.00000, 0.00000)
Gd: (0.50000, 0.50000, 0.50000)
Rh: (0.00000, 0.50000, 0.25000)
Rh: (0.00000, 0.50000, 0.75000)
Rh: (0.50000, 0.00000, 0.25000)
Rh: (0.50000, 0.00000, 0.75000)
Si: (0.00000, 0.00000, 0.37742)
Si: (0.00000, 0.00000, 0.62258)
Si: (0.50000, 0.50000, 0.87742)
Si: (0.50000, 0.50000, 0.12258)

The phonon band structure, shown in Fig. 12, confirms the dynamical stability of the system, with no imaginary phonon frequencies observed.

TABLE V. A crystal structure of studied compounds, used in atomistic spin-dynamics simulations. Specifically, a , c , V , and z are the tetragonal lattice constants, the volume of the unit cell, and the free parameter of the Si ions' position, respectively.

Ln	Ho	Dy	Nd	Sm	Pr	Tb	Gd
a (Å)	4.015	4.022	4.069	4.055	4.079	4.037	4.045
c (Å)	9.89	9.90	10.11	10.04	9.986	9.95	9.98
V (Å ³)	159.4	160.1	167.4	165.1	166.1	162.1	163.3
z	0.3765	0.375	0.375	0.375	0.375	0.375	0.375

FIG. 13. Spin, lattice, and electron temperatures in HC3TM for GdRh₂Si₂.

APPENDIX C: ATOMISTIC SPIN-LATTICE DYNAMICS SIMULATIONS

Coupled atomistic spin-lattice dynamics simulations are performed, using Langevin dynamics, similarly to Refs. [2,7,30]. In addition to spin dynamics governed by Eq. (2), the lattice dynamics is described by

$$\frac{d\mathbf{u}_k}{dt} = \mathbf{v}_k, \quad (\text{C1})$$

$$\frac{d\mathbf{v}_k}{dt} = \frac{\mathbf{F}_k}{M_k} + \frac{\mathbf{F}_k^{fl}}{M_k} - \nu \mathbf{v}_k, \quad (\text{C2})$$

where the lattice damping constant is denoted ν , and atomic displacements and velocities are given by \mathbf{u}_k , \mathbf{v}_k , respectively. The force at site k is defined by $\mathbf{F}_k = -\partial H_{\text{SLD}}/\partial \mathbf{u}_k$. The spin-lattice Hamiltonian H_{SLD} is a sum of magnetic contributions given in Eq. (1) and lattice contribution $H_{\text{SLD}} = H + H_{\text{LL}}$, where H_{LL} is

$$H_{\text{LL}} = \frac{1}{2} \sum_{kl} \Phi_{kl}^{\mu\nu} u_k^\mu u_l^\nu + \frac{1}{2} \sum_k M_k v_k^\mu v_k^\mu, \quad (\text{C3})$$

where $\Phi_{kl}^{\mu\nu}$ is the force constant tensor, and M_k is the mass of atom k .

In these types of Langevin simulations, one employs stochastic fields \mathbf{F}_k^{fl} as white noise with properties $\langle F_{i,\mu}^{fl}(t) F_{j,\nu}^{fl}(t') \rangle = 2D_L \delta_{kl} \delta_{\mu\nu} \delta(t - t')$. In our simulations, we use $D_L = \nu M k_B T$ (see, e.g., Refs. [2,7,30]).

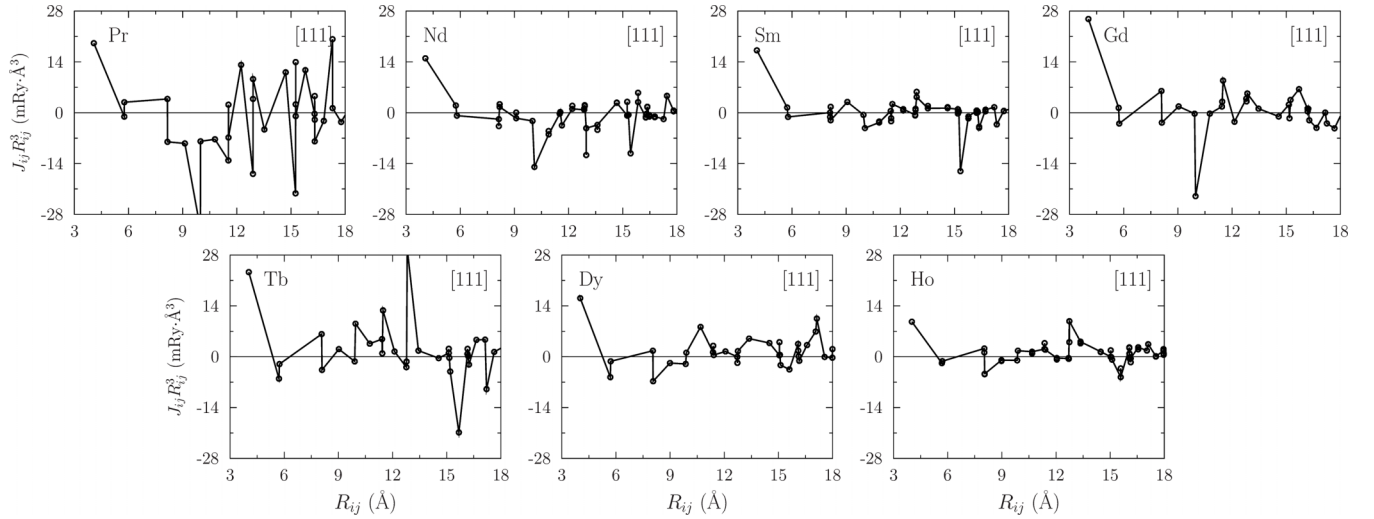


FIG. 14. Dependence of the Heisenberg interaction between the Ln spins on the distance between them for all studied rare-earth compounds calculated using the hutsepot code. The y-axis shows the quantity $J_{ij}R_{ij}^3$, which experiences long-range oscillations in space, similarly to the RKKY mechanism in three-dimensional systems.

The lattice temperature T_l for the HC3TM is calculated from the average kinetic energy of the lattice vibrations, $\langle E_l^{\text{kin}} \rangle / k_B$.

APPENDIX D: CRYSTAL STRUCTURE

Table V displays the crystal structure of the studied compounds.

APPENDIX E: SPIN, ELECTRON, AND LATTICE TEMPERATURES IN HC3TM

The dynamics of spin, lattice, and electron temperatures in HC3TM for GdRh_2Si_2 is presented in Fig. 13. One can notice that the electron temperature is rising first, followed closely by the lattice temperature, which is in line with pre-

vious experimental studies [12], where the thermalization of electronic and lattice temperatures was observed during the first picoseconds after the laser pulse. The rise of T_e and T_l is then followed by a much slower rise of the spin temperature. The slow rise of spin temperature, in comparison, for example, with $3d$ ferromagnets [2,7], is explained by a very low Gilbert damping used in this work, which in the HC3TM model is responsible for a transfer of heat between electronic and spin subsystems [2,7], as well as being influenced by exchange interactions. Therefore, the difference in temperatures dynamics, in comparison with $3d$ ferromagnets [2,7] previously studied in HC3TM, is explained by different Gilbert damping values, different force constants, and exchange interactions, which influence magnetization dynamics and, therefore, the temperatures “measured” during the atomistic spin-lattice dynamics simulations.

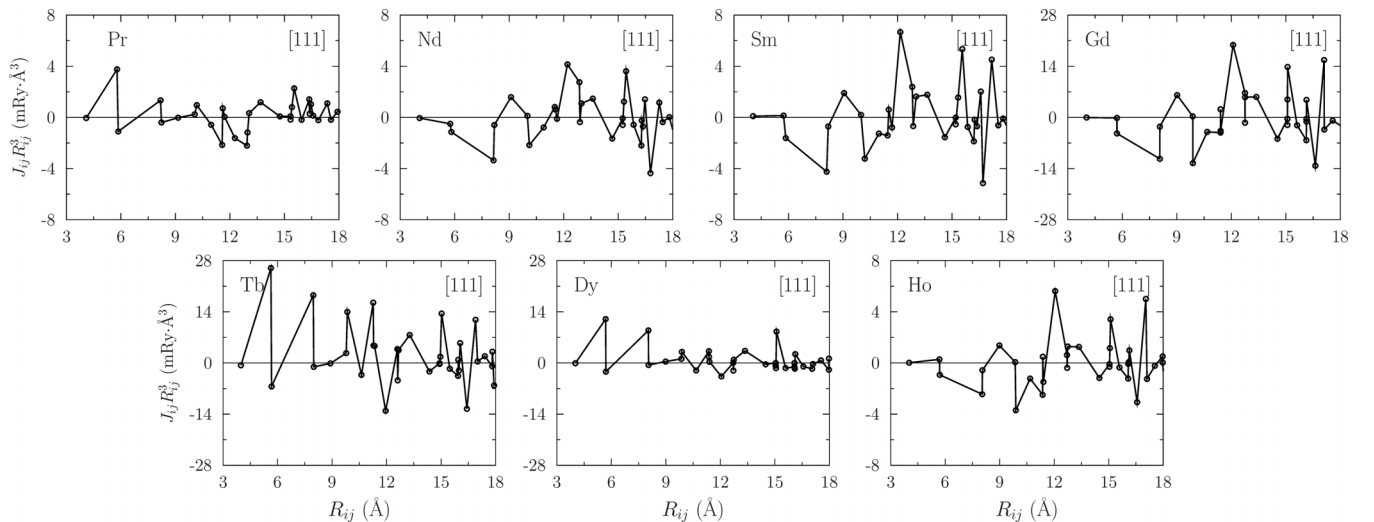


FIG. 15. Dependence of the Heisenberg interaction between the Ln spins on the distance between them for all studied rare-earth compounds calculated using the RSPt code. The y-axis shows the quantity $J_{ij}R_{ij}^3$, which experiences long-range oscillations in space, similarly to the RKKY mechanism in three-dimensional systems.

APPENDIX F: LONG-RANGE CHARACTER OF HEISENBERG INTERACTIONS

Here, we consider the long-range behavior of Heisenberg magnetic interactions in all studied rare-earth systems. In

Figs. 14 and 15, the distance dependence is shown for the Heisenberg interaction multiplied with a cube of distance. Real-space oscillations of this quantity typically indicate the RKKY mechanism, well-known for simple 3d ferromagnetic metals [43].

-
- [1] E. Beaurepaire, J.-C. Merle, A. Daunois, and J.-Y. Bigot, Ultrafast spin dynamics in ferromagnetic nickel, *Phys. Rev. Lett.* **76**, 4250 (1996).
- [2] M. Pankratova, I. P. Miranda, D. Thonig, M. Pereiro, E. Sjöqvist, A. Delin, O. Eriksson, and A. Bergman, Heat-conserving three-temperature model for ultrafast demagnetization in nickel, *Phys. Rev. B* **106**, 174407 (2022).
- [3] D. Zahn, F. Jakobs, Y. W. Windsor, H. Seiler, T. Vasileiadis, T. A. Butcher, Y. Qi, D. Engel, U. Atxitia, J. Vorberger, and R. Ernstorfer, Lattice dynamics and ultrafast energy flow between electrons, spins, and phonons in a 3d ferromagnet, *Phys. Rev. Res.* **3**, 023032 (2021).
- [4] T. Griepe and U. Atxitia, Evidence of electron-phonon mediated spin flip as driving mechanism for ultrafast magnetization dynamics in 3d ferromagnets, *Phys. Rev. B* **107**, L100407 (2023).
- [5] B. Frietsch, A. Donges, R. Carley, M. Teichmann, J. Bowlan, K. Döbrich, K. Carva, D. Legut, P. M. Oppeneer, U. Nowak, and M. Weinelt, The role of ultrafast magnon generation in the magnetization dynamics of rare-earth metals, *Sci. Adv.* **6**, eabb1601 (2020).
- [6] M. Teichmann, B. Frietsch, K. Döbrich, R. Carley, and M. Weinelt, Transient band structures in the ultrafast demagnetization of ferromagnetic gadolinium and terbium, *Phys. Rev. B* **91**, 014425 (2015).
- [7] M. Pankratova, I. Miranda, M. Pereiro, E. Sjöqvist, A. Delin, P. Scheid, O. Eriksson, and A. Bergman, Coupled atomistic spin-lattice simulations of ultrafast demagnetization in 3d ferromagnets, *Sci. Rep.* **14**, 8138 (2024).
- [8] Q. Remy, Ultrafast magnetization reversal in ferromagnetic spin valves: An s - d model perspective, *Phys. Rev. B* **107**, 174431 (2023).
- [9] D. Gupta, M. Pankratova, M. Riepp, M. Pereiro, B. Sanyal, S. Ershadrad, M. Hehn, N. Pontius, C. Schüßler-Langeheine, N. Berggaard *et al.*, Tuning ultrafast demagnetization with ultrashort spin polarized currents in multi-sublattice ferrimagnets, *Nat. Commun.* **16**, 3097 (2025).
- [10] Y. W. Windsor, S.-E. Lee, D. Zahn, V. Borisov, D. Thonig, K. Kliemt, A. Ernst, C. Schüßler-Langeheine, N. Pontius, U. Staub *et al.*, Exchange scaling of ultrafast angular momentum transfer in 4f antiferromagnets, *Nat. Mater.* **21**, 514 (2022).
- [11] S.-E. Lee, Y. W. Windsor, D. Zahn, A. Kraiker, K. Kummer, K. Kliemt, C. Krellner, C. Schüßler-Langeheine, N. Pontius, U. Staub, D. V. Vyalikh, A. Ernst, and L. Rettig, Controlling 4f antiferromagnetic dynamics via itinerant electronic susceptibility, *Phys. Rev. Res.* **6**, 043019 (2024).
- [12] S.-E. Lee, Y. W. Windsor, A. Fedorov, K. Kliemt, C. Krellner, C. Schüßler-Langeheine, N. Pontius, M. Wolf, U. Atxitia, D. V. Vyalikh *et al.*, Robust magnetic order upon ultrafast excitation of an antiferromagnet, *Adv. Mater. Inter.* **9**, 2201340 (2022).
- [13] N. Thielemann-Kühn, D. Schick, N. Pontius, C. Trabant, R. Mitzner, K. Hollmack, H. Zabel, A. Föhlisch, and C. Schüßler-Langeheine, Ultrafast and energy-efficient quenching of spin order: Antiferromagnetism beats ferromagnetism, *Phys. Rev. Lett.* **119**, 197202 (2017).
- [14] J. H. Mentink, J. Hellsvik, D. V. Afanasiev, B. A. Ivanov, A. Kirilyuk, A. V. Kimel, O. Eriksson, M. I. Katsnelson, and T. Rasing, Ultrafast spin dynamics in multisublattice magnets, *Phys. Rev. Lett.* **108**, 057202 (2012).
- [15] J. M. Wills and B. R. Cooper, Synthesis of band and model hamiltonian theory for hybridizing cerium systems, *Phys. Rev. B* **36**, 3809 (1987).
- [16] J. Wills *et al.*, *Full-Potential Electronic Structure Method* (Springer-Verlag, Berlin, 2010), p. 167.
- [17] M. Geilhufe, S. Achilles, M. A. Köbis, M. Arnold, I. Mertig, W. Hergert, and A. Ernst, Numerical solution of the relativistic single-site scattering problem for the Coulomb and the Mathieu potential, *J. Phys.: Condens. Matter* **27**, 435202 (2015).
- [18] M. Hoffmann, A. Ernst, W. Hergert, V. N. Antonov, W. A. Adeagbo, M. R. Geilhufe, and H. Ben Hamed, Magnetic and electronic properties of complex oxides from first-principles, *Phys. Status Solidi B* **257**, 1900671 (2020).
- [19] V. I. Anisimov, J. Zaanen, and O. K. Andersen, Band theory and mott insulators: Hubbard U instead of stoner I, *Phys. Rev. B* **44**, 943 (1991).
- [20] A. I. Liechtenstein, M. I. Katsnelson, V. P. Antropov, and V. A. Gubanov, Local spin density functional approach to the theory of exchange interactions in ferromagnetic metals and alloys, *J. Magn. Magn. Mater.* **67**, 65 (1987).
- [21] A. Szilva, Y. Kvashnin, E. A. Stepanov, L. Nordström, O. Eriksson, A. I. Liechtenstein, and M. I. Katsnelson, Quantitative theory of magnetic interactions in solids, *Rev. Mod. Phys.* **95**, 035004 (2023).
- [22] B. Skubic, J. Hellsvik, L. Nordström, and O. Eriksson, A method for atomistic spin dynamics simulations: Implementation and examples, *J. Phys.: Condens. Matter* **20**, 315203 (2008).
- [23] L. Landau and E. Lifshitz, Theory of the dispersion of magnetic permeability in ferromagnetic bodies, *Phys. Z. Sowjetunion* **8**, 153 (1935).
- [24] T. Gilbert, A phenomenological theory of damping in ferromagnetic materials, *IEEE Trans. Magn.* **40**, 3443 (2004).
- [25] A. Secchi, A. I. Liechtenstein, and M. I. Katsnelson, Magnetic interactions in strongly correlated systems: Spin and orbital contributions, *Ann. Phys.* **360**, 61 (2015).
- [26] O. Eriksson, A. Bergman, L. Bergqvist, and J. Hellsvik, *Atomistic Spin Dynamics: Foundations and Applications* (Oxford University Press, Oxford, UK, 2017).
- [27] P.-W. Ma, S. L. Dudarev, A. A. Semenov, and C. H. Woo, Temperature for a dynamic spin ensemble, *Phys. Rev. E* **82**, 031111 (2010).

- [28] L. Bergqvist and A. Bergman, Realistic finite temperature simulations of magnetic systems using quantum statistics, *Phys. Rev. Mater.* **2**, 013802 (2018).
- [29] B. Frietsch, J. Bowlan, R. Carley, M. Teichmann, S. Wienholdt, D. Hinzke, U. Nowak, K. Carva, P. M. Oppeneer, and M. Weinelt, Disparate ultrafast dynamics of itinerant and localized magnetic moments in gadolinium metal, *Nat. Commun.* **6**, 8262 (2015).
- [30] J. Hellsvik, D. Thonig, K. Modin, D. Iușan, A. Bergman, O. Eriksson, L. Bergqvist, and A. Delin, General method for atomistic spin-lattice dynamics with first-principles accuracy, *Phys. Rev. B* **99**, 104302 (2019).
- [31] K. Mishra, A. Ciuciulkaite, M. Zapata-Herrera, P. Vavassori, V. Kapaklis, T. Rasing, A. Dmitriev, A. Kimel, and A. Kirilyuk, Ultrafast demagnetization in a ferrimagnet under electromagnetic field funneling, *Nanoscale* **13**, 19367 (2021).
- [32] U. Atxitia, O. Chubykalo-Fesenko, J. Walowski, A. Mann, and M. Münzenberg, Evidence for thermal mechanisms in laser-induced femtosecond spin dynamics, *Phys. Rev. B* **81**, 174401 (2010).
- [33] S. Jana, R. S. Malik, Y. O. Kvashnin, I. L. M. Loht, R. Knut, R. Stefanuik, I. Di Marco, A. N. Yaresko, M. Ahlberg, J. Åkerman, R. Chimata, M. Battiato, J. Söderström, O. Eriksson, and O. Karis, Analysis of the linear relationship between asymmetry and magnetic moment at the M edge of $3d$ transition metals, *Phys. Rev. Res.* **2**, 013180 (2020).
- [34] K. Momma and F. Izumi, *Vesta 3* for three-dimensional visualization of crystal, volumetric and morphology data, *J. Appl. Crystallogr.* **44**, 1272 (2011).
- [35] K. Kliemt and C. Krellner, Single crystal growth and characterization of GdRh_2Si_2 , *J. Cryst. Growth* **419**, 37 (2015).
- [36] G. Kresse and J. Furthmüller, Efficient iterative schemes for *ab initio* total-energy calculations using a plane-wave basis set, *Phys. Rev. B* **54**, 11169 (1996).
- [37] A. Togo, Y. Inoue, and I. Tanaka, Phonon structure of titanium under shear deformation along $\{10\bar{1}2\}$ twinning mode, *Phys. Rev. B* **102**, 024106 (2020).
- [38] G. Kresse and D. Joubert, From ultrasoft pseudopotentials to the projector augmented-wave method, *Phys. Rev. B* **59**, 1758 (1999).
- [39] J. P. Perdew, K. Burke, and M. Ernzerhof, Generalized gradient approximation made simple, *Phys. Rev. Lett.* **77**, 3865 (1996).
- [40] G. Kotliar, S. Y. Savrasov, K. Haule, V. S. Oudovenko, O. Parcollet, and C. A. Marianetti, Electronic structure calculations with dynamical mean-field theory, *Rev. Mod. Phys.* **78**, 865 (2006).
- [41] A. Liechtenstein, V. I. Anisimov, and J. Zaanen, Density-functional theory and strong interactions: Orbital ordering in Mott-Hubbard insulators, *Phys. Rev. B* **52**, R5467(R) (1995).
- [42] M. Güttler, A. Generalov, M. Otrokov, K. Kummer, K. Kliemt, A. Fedorov, A. Chikina, S. Danzenbächer, S. Schulz, E. V. Chulkov *et al.*, Robust and tunable itinerant ferromagnetism at the silicon surface of the antiferromagnet GdRh_2Si_2 , *Sci. Rep.* **6**, 24254 (2016).
- [43] R. Cardias, A. Szilva, A. Bergman, I. D. Marco, M. I. Katsnelson, A. I. Liechtenstein, L. Nordström, A. B. Klautau, O. Eriksson, and Y. O. Kvashnin, The bethe-slater curve revisited; new insights from electronic structure theory, *Sci. Rep.* **7**, 4058 (2017).